SCIENTIFIC REPORTS

OPEN

Chiral spin ordering of electron gas in solids with broken time reversal symmetry

K. S. Denisov[1,2], I. V. Rozhansky[1,2], N. S. Averkiev[1] & E. Lähderanta[2]

In this work we manifest that an electrostatic disorder in conducting systems with broken time reversal symmetry universally leads to a chiral ordering of the electron gas giving rise to skyrmion-like textures in spatial distribution of the electron spin density. We describe a microscopic mechanism underlying the formation of the equilibrium chiral spin textures in two-dimensional systems with spin-orbit interaction and exchange spin splitting. We have obtained analytical expressions for spin-density response functions and have analyzed both local and non-local spin response to electrostatic perturbations for systems with parabolic-like and Dirac electron spectra. With the proposed theory we come up with a concept of controlling spin chirality by electrical means.

The concept of spin chirality constitutes a substantial part of modern condensed matter physics. It is widely applied to strongly correlated electron systems[1–4] when interpreting the fractional statistics[5–7], or chiral spin liquids[8–11] in terms of an effective gauge field. Remarkably, a finite spin chirality induces a gauge invariant magnetic flux, which is an experimentally observable quantity[1]. It was shown that the chirality driven magnetic field affects electron transport in the very same way as the ordinary magnetic field does[12,13] leading to the Hall response, the phenomenon currently referred as the topological Hall effect[14–17]. Naturally, to get an experimental access to the variety of spin chirality driven phenomena an efficient tool for creating a chiral spin order is needed. One way towards this goal is to focus on materials possessing exotic spin textures, such as magnetic skyrmions[18–21], or merons[22]. Magnetic skyrmion is a topologically nontrivial configuration of the magnetization stabilized by a spin-orbit interaction in systems with broken inversion symmetry[23,24]; along with the fact that it triggers a number of peculiar effects, such as the skyrmion Hall effect[25], this quasiparticle attracts a great interest due to possible applications in the race-track memory devices[26,27]. Still, exploring the physical mechanisms behind the emergence of spin chirality in solids remains challenging and is of high fundamental interest.

In this paper we show that in systems with broken time reversal symmetry ($\mathcal{T}$-symmetry) a chiral spin order of electron gas is universally induced by an electrostatic disorder, which is an inherent property of any real solid. We argue that numerous crystal imperfections, such as residue impurities or surface defects appear to be a source of local chiral spin ordering of electrons. This effect is more pronounced for an electron gas with stronger spin-orbit interaction (SOI). Naturally, various magnetic systems such as magnetic topological insulators (TI)[28–31], Rashba magnetic layers[32–35] or dilute magnetic semiconductors (DMS)[36–41] are in fact flooded by chiral spin textures pinned to structural defects. This effect opens up a novel concept of an experimental research of spin chirality driven phenomena.

General Theory

In our work we focus on two-dimensional degenerate electron gas (2DEG). We introduce an effective 'magnetic field' acting on an electron spin:

$$\boldsymbol{B}_k = (\lambda k \cos(\chi\varphi_k + \gamma),\ \lambda k \sin(\chi\varphi_k + \gamma),\ h), \tag{1}$$

where $\boldsymbol{k} = (k, \varphi_k)$ is a 2D momentum with magnitude k and polar angle φ_k. The parameter $h > 0$ describes the out-of-plane component leading to the carrier spin splitting at $k = 0$, it is thus responsible for the violation of $\mathcal{T}$-symmetry. The in-plane components of $\boldsymbol{B}_k$ represent linear in k terms due to SOI, λ is the SOI coupling constant. The SOI parameters $\chi = \pm 1$ (helicity) and γ (vorticity) cover different types of the SOI interaction.

[1]Ioffe Institute, St.Petersburg, 194021, Russia. [2]Lappeenranta-Lahti University of Technology, FI-53851, Lappeenranta, Finland. Correspondence and requests for materials should be addressed to K.S.D. (email: denisokonstantin@gmail.com)
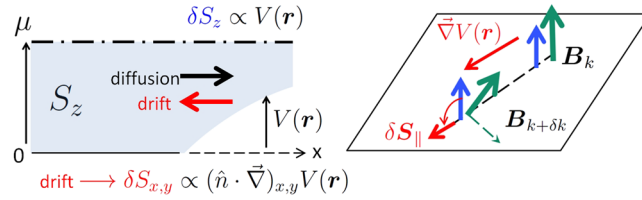
Figure 1. The physical picture behind the emergence of an equilibrium chiral spin pattern of the electron gas. The in-plane spin arises from the precession due to drift electron flow.

Let us further assume an electrostatic disorder due to various defects present in the system. When $\mathcal{T}$-symmetry is broken the spatial distribution of the equilibrium electron spin density follows the inhomogeneity of the electrostatic potential $V(\mathbf{r})$ (the notation $\mathbf{r} = (x, y)$ stands for 2D radius vector, we do not take into account variation of the potential along z-axis perpendicular to the motion plane). Indeed, at $h \neq 0$ there is a nonzero electron spin polarization directed perpendicular to the motion plane. A local variation of the potential magnitude $V(\mathbf{r})$ leads to a spatial redistribution of electrons and, hence, to the change of both 2DEG charge density and spin density δS_z component along z. When SOI is present ($\lambda \neq 0$) the in-plane components of the spin density $\delta S_{x,y}$ appear as well, so the induced spin response $\delta \mathbf{S}$ acquires a chiral spatial pattern forming skyrmion-like spin textures.

Let us notice that the mechanics behind the appearance of $\delta S_{x,y}$ in response to an electrostatic potential has a peculiar character, and it differs from that for δS_z. Since there is no net in-plane spin polarization at a spatially uniform electrostatic potential, $\delta S_{x,y}$ appears only due to its gradient. One can consider the following quasiclassical picture, see Fig. 1. An electron with initial momentum $\mathbf{k}$ and spin $\mathbf{S}_k$ co-aligned with the direction of $\mathbf{B}_k$ moves along a certain trajectory. Due to the electrostatic potential gradient $\overrightarrow{\nabla} V(\mathbf{r})$ the carrier momentum is changed $\mathbf{k} + \delta \mathbf{k}$, thus changing the tilt of $\mathbf{B}_{k+\delta k}$, which in-plane components are coupled with momentum. This process triggers the precession of the electron spin around the new direction of the effective magnetic field creating an excessive in-plane spin density. In the thermodynamic equilibrium there is no net current as the drift and diffusion electron flows are compensated everywhere. However, when the time-reversal symmetry is broken the two flows have different effect on an electron spin. Indeed, while the diffusion flow does not affect the in-plane spin components, the drift flow associated with the change of the electron momentum leads to the emergence of an in-plane spin according to the arguments given above. This difference between drift and diffusion flows results in the accumulation of 2DEG spin density $\delta S_{x,y}$ in the equilibrium.

The emergence of the spin textures due to spatial variation of the electrostatic potential is described by static spin-density response functions:

$$\mathcal{F}_\alpha(\mathbf{q}) = \sum_{k,s,s'} \langle u_k^s | \hat{S}_\alpha | u_{k+q}^{s'} \rangle \langle u_{k+q}^{s'} | u_k^s \rangle \frac{f_k^s - f_{k+q}^{s'}}{\varepsilon_k^s - \varepsilon_{k+q}^{s'} + i0}, \tag{2}$$

where $\hat{S}_\alpha$ is a spin projection operator for $\alpha = (x, y, z)$ axis, index $s = \pm$ denotes two electron subbands, ε_k^s and $|u_k^s\rangle$ are the energy and the Bloch amplitude of an electron in the state $(\mathbf{k}, s)$, f_k^s is the equilibrium distribution function. Using the functions $\mathcal{F}_\alpha(\mathbf{q})$ one can analyze the spin density $\delta \mathbf{S}(\mathbf{r})$ emerging in 2DEG in the vicinity of a doping center or a defect with a potential $V(\mathbf{r})$:

$$\delta S_\alpha(\mathbf{r}) = \int \frac{d\mathbf{q}}{(2\pi)^2} e^{i\mathbf{q}\mathbf{r}} \mathcal{F}_\alpha(\mathbf{q}) V(\mathbf{q}), \tag{3}$$

where $V(\mathbf{q})$ is the Fourier transform of $V(\mathbf{r})$, the electron-electron interaction is neglected. In particular, the functions $\mathcal{F}_\alpha(\mathbf{q})$ allow us to identify whether the spin response is local or extends beyond the localization radius of the potential due to the wave properties of 2DEG.

Let us point out a few general features of the spin response. As has been mentioned above, z-component of the 2DEG spin density is analogous to the 2DEG charge density, so if there is no spatial dispersion δS_z locally couples with the potential $\delta S_z(\mathbf{r}) = \varkappa_z V(\mathbf{r})$. On the contrary, the in-plane spin components driven by the precession mechanism illustrated by Fig. 1 are induced by the gradient of $V(\mathbf{r})$. In the case of a local response this coupling takes the form $\delta S_{x,y} = \varkappa_\parallel (\hat{n} \cdot \overrightarrow{\nabla})_{x,y} V(\mathbf{r})$, where $\hat{n}$ is a rotation matrix determined by SOI type (see Eq. 4). The coefficients $\varkappa_{z,\parallel}$ are determined by a carrier spectrum. Since the Fourier transform of $\overrightarrow{\nabla} V(\mathbf{r})$ is $i\mathbf{q}V(\mathbf{q})$, we conclude that $\mathcal{F}_{x,y}(\mathbf{q})$ are purely imaginary, we express them as

$$\mathcal{F}_{x,y}(\mathbf{q}) = i(\hat{n} \mathbf{e}_q)_{x,y} \mathcal{F}_\parallel(q), \qquad \hat{n} = \begin{pmatrix} \sin\gamma & (-1)^\chi \cos\gamma \\ -\cos\gamma & (-1)^\chi \sin\gamma \end{pmatrix}, \tag{4}$$

where the real function $\mathcal{F}_\parallel(q)$ does not depend on $\mathbf{q}$ direction $\mathbf{e}_q = \mathbf{q}/q$. Naturally, $\mathcal{F}_\parallel(q) \propto q$ at $q \to 0$.

When there is some spatial inhomogeneity of crystalline structure the electron gas acquires a local spin chirality. For an axially symmetric potential $V(r)$ the excessive spin density $\delta \mathbf{S}(\mathbf{r})$ profile has a shape:
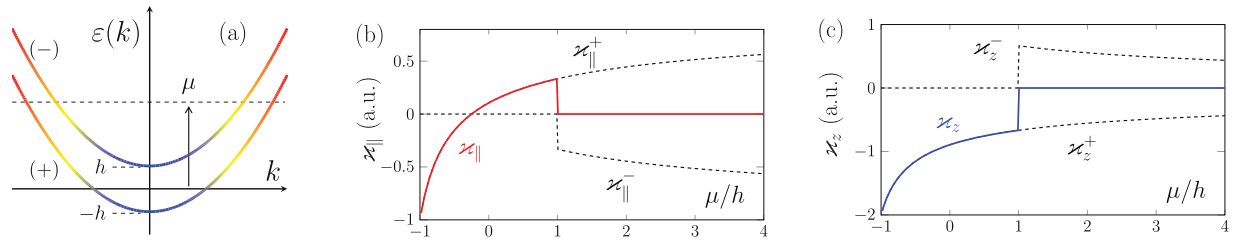
Figure 2. (a) Parabolic-like electron spectrum Eq. 6, (b,c) the dependence of $\varkappa_{\parallel,z}$ on μ for $\xi = 0.5$.

$$\delta \boldsymbol{S}(\boldsymbol{r}) = \begin{pmatrix} \delta S_{\parallel}(r)\cos(\chi\varphi_r + \gamma') \\ \delta S_{\parallel}(r)\sin(\chi\varphi_r + \gamma') \\ \delta S_z(r) \end{pmatrix}, \qquad \delta S_{z,\parallel}(r) = \int \frac{q dq}{2\pi} J_{0,1}(qr) \mathcal{F}_{z,\parallel}(q) V(q),$$

(5)

where $\boldsymbol{r} = (r, \varphi_r)$, $\delta S_{\parallel}$, δS_z depend on r, $J_{0,1}$ are Bessel's functions of the zeroth and first order, respectively, $\gamma' = \gamma + \pi/2$. The emerging chiral spin cloud is similar to a skyrmion for $\chi = 1$, or to an antiskyrmion for $\chi = -1$. The fact that the helicity γ' of the real space spin rotation is shifted by $\pi/2$ with respect to γ in k-space reflects the spin precession mechanism.

The details of chiral spin response naturally depend on a carrier band structure $\varepsilon_k^{\pm}$. To analyze general features of the studied phenomena we consider the two most widely used models with different particular symmetry properties. Namely, we calculate $\mathcal{F}_{z,\parallel}(q) = \mathcal{F}_{z,\parallel}^+ + \mathcal{F}_{z,\parallel}^-$, which is a sum of the responses of two subbands (see Supplementary Appendix B), and analyze the electron spin density for parabolic-like and Dirac electron spectra.

Parabolic-like Spectrum

Let us assume the following Hamiltonian H_k and the energy spectrum ε_k^s:

$$H_k = \frac{k^2}{2m} - \boldsymbol{B}_k \cdot \hat{\boldsymbol{\sigma}}, \qquad \varepsilon_k^{\pm} = \frac{k^2}{2m} \mp B_k, \qquad B_k = \sqrt{h^2 + (\lambda k)^2},$$

(6)

where m is the effective mass in the absence of B_k (we assume $\hbar = 1$). In this paper we take the parameter $\xi = m\lambda^2/h < 1$. The spectrum of the system is shown in Fig. 2a, the color within each subband indicates the magnitude of $\zeta_s = \lambda k_s/h$, which has a meaning of spin inclination into the plane of the carrier motion (blue color corresponds to $\zeta_s \ll 1$, red color indicates $\zeta_s \gg 1$). We have obtained analytic expressions for the spin-density response functions $\mathcal{F}_{z,\parallel}$ with the spectrum given by Eq. 6. As the formulas are rather cumbersome, we provide them in the Supplementary Appendix A (the details of the calculations are given in the Supplementary Appendix B). Importantly, $\mathcal{F}_{z,\parallel}^{\pm}$ within each subband are decomposed into a sum of intra- and interband contributions $\mathcal{F}_{z,\parallel}^{\pm} = \mathcal{F}_{z,\parallel}^{\pm\pm} + \mathcal{F}_{z,\parallel}^{\pm\mp}$ with the interband terms exhibiting an additional coupling $\mathcal{F}_z^{\pm\mp}(q) = (2m\lambda/q)\mathcal{F}_{\parallel}^{\pm\mp}(q)$.

Let us firstly consider the local coupling regime, when $\delta S_{x,y}(\boldsymbol{r}) = \varkappa_{\parallel}(\hat{n} \cdot \overrightarrow{\nabla})_{x,y} V(\boldsymbol{r})$ and $\delta S_z(\boldsymbol{r}) = \varkappa_z V(\boldsymbol{r})$. The coefficients $\varkappa_{z,\parallel} = \varkappa_{z,\parallel}^+ + \varkappa_{z,\parallel}^-$ found from the limiting behavior of $\mathcal{F}_{z,\parallel}^{\pm}$ at $q \to 0$ are given by

$$\varkappa_z^s = -s\frac{m}{4\pi}\frac{\Theta[\mu + sh]}{\sqrt{1 + \zeta_s^2} - s\xi}, \qquad \varkappa_{\parallel}^s = \frac{s}{8\pi\lambda}\left(1 - \frac{1}{\sqrt{1 + \zeta_s^2} - s\xi}\right)\Theta[\mu + sh].$$

(7)

Let us mention that the coefficient $\varkappa_z^{\pm}$ is the product of the electron density of states and z-projection of spin taken at the Fermi energy μ. The dependence of $\varkappa_{z,\parallel}$ on μ is shown in Fig. 2b,c. We note that nonzero spin response is observed only when the upper subband is empty ($\mu < h$). This result is an inherent property of the considered model; the background spin density $S_z^0 = (mh/4\pi)$ remains constant at $\mu > h$.

As follows from the explicit expressions for $\mathcal{F}_{z,\parallel}^{\pm}$, the local coupling regime occurs when the Fourier components of $V(\boldsymbol{q})$ are localized within $q \ll \min[k_{\pm}, a_0^{-1}]$, where $a_0 = \lambda/2h$. For these values the response functions $\mathcal{F}_z$, $\mathcal{F}_{\parallel}/q$ have a weak dependence on q, which means no spatial dispersion and, thus, the absence of non-locality in the response. Note, that, apart from the Fermi wavevector $k_{\pm}$, there is a second spatial scale $a_0 = \lambda/2h$, which controls the spatial dispersion of the spin response. This scale is associated with the precession mechanism for the in-plane spin generation.

We proceed with considering the non-local spin response, firstly for the case when only the $(+)$ subband is populated ($-h < \mu < h$). The dependence of $\mathcal{F}_{z,\parallel}^+$, and its partial contributions $\mathcal{F}_{z,\parallel}^{+\pm}$ on $q/2k_+$ is shown in Fig. 3(a,b). As we have discussed above, the response functions at $q \to 0$ behave as $\mathcal{F}_z^+ \approx \varkappa_z^+$, $\mathcal{F}_{\parallel}^+ \approx \varkappa_{\parallel}^+ q$. Another general trend is that the intra-$\mathcal{F}_{z,\parallel}^{++}$ and interband $\mathcal{F}_{z,\parallel}^{+-}$ terms have an opposite sign and, thus, tend to cancel each other. The spatial profile $\delta S_{z,\parallel}(r)$ induced around a repulsive short range potential $V(r) = \alpha_0\delta(\boldsymbol{r})$ is shown in Fig. 3c. The largest spin response appears within the Fermi wavelength ($2k_+r \lesssim 2$). Far apart from the center $\delta S_{z,\parallel}(r)$ decrease exhibiting the Friedel oscillations with the period $2k_+$ (see inset in Fig. 3).
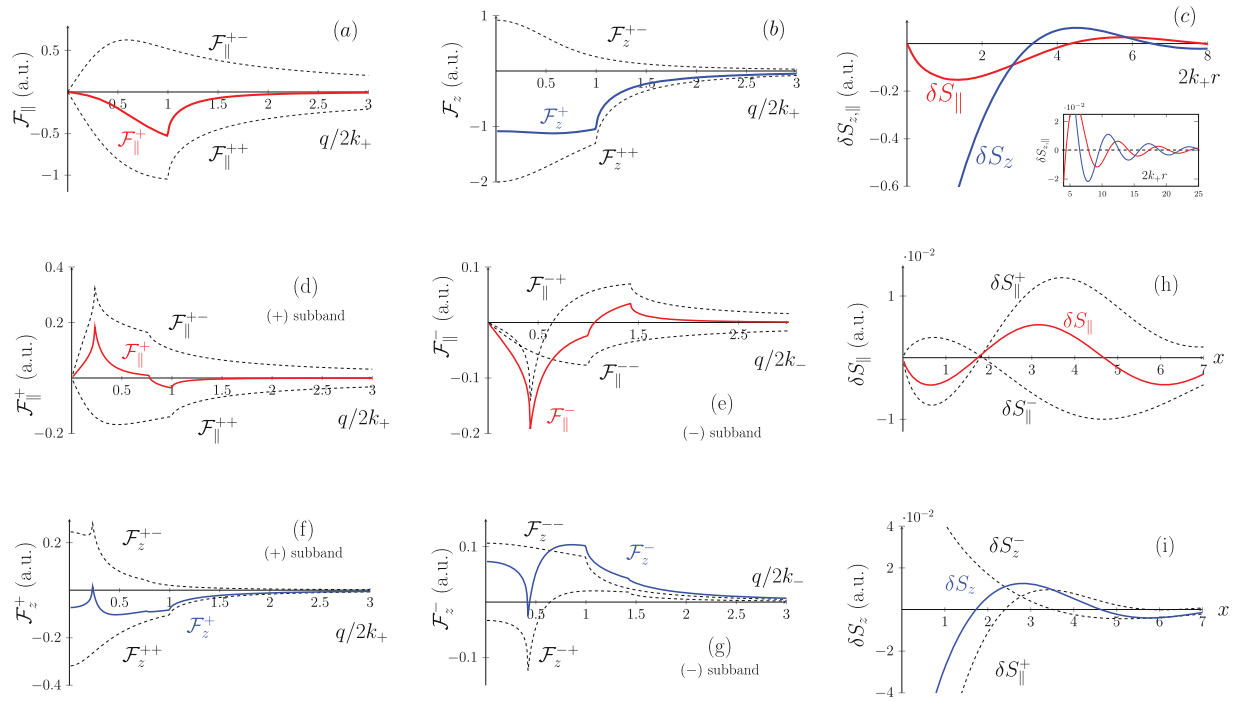
Figure 3. (a–c) The dependence of $\mathcal{F}^+_{z,\parallel}$ on $q/2k_+$, and $\delta S_{z,\parallel}$ on $2k_+r$ in case of one filled spin subband ($\xi = 0.5$, $\mu = -0.4h$, $\zeta_+ = 1$), (d–g) the dependence of $\mathcal{F}^\pm_{z,\parallel}$ on $q/2k_\pm$, (h,i) the dependence of $\delta S_{z,\parallel}$ on $x = 2(\sqrt{2m\mu})r$ in case of two filled spin subbands, the parameters are $\mu = 3.5h$, $\xi = 0.5$, $\zeta_+ = 2.5$, $\zeta_- = 1.4$.
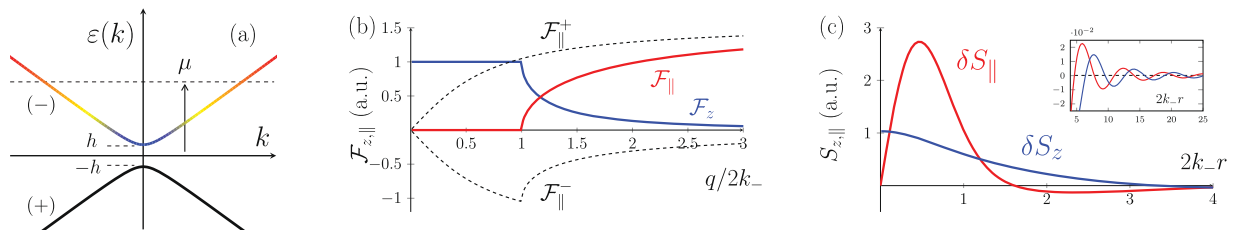

Figure 4. (a) Dirac electron spectrum, (b) the dependence of $\mathcal{F}^\pm_{z,\parallel}$ on $q/2k_-$, (c) the dependence of $\delta S_{\parallel,z}$ on $2k_-r$, the inset shows the Friedel's oscillations. The parameters are $\mu = 2h$, $\zeta_- = 1.7$, $ak_- = 0.3$.

Let us now consider the case $\mu > h$ when both spin subbands are populated. Although the local spin response is absent in this case ($\varkappa_{z,\parallel} = 0$), the effect of spatial dispersion restores the chiral spin pattern. Shown in Fig. 3(d–g) are the obtained spin response functions $\mathcal{F}^\pm_{z,\parallel}(q)$. We note that the intraband terms $\mathcal{F}^{\pm\pm}_{z,\parallel}$ for both subbands exhibit a single spike at $q = 2k_\pm$. What is more interesting is the double-spike structure of the interband terms $\mathcal{F}^{\pm\mp}_{z,\parallel}$ driven by two nesting vectors connecting two distinct subbands of the Fermi surface. The presence of the two different spatial scales $k_\pm$ along with a complex structure of interband transitions lead to quite a peculiar spin response in the real space. In Fig. 3h,i we demonstrate $\delta S_{z,\parallel}(r)$ for the short range potential $V(q) = \alpha_0$. The spatial scale is given in units of $x = k_F r$, where k_F is the averaged Fermi wavevector. The Friedel oscillations clearly visible at large distances from the centre $x \gg 1$ are now formed by the superposition of oscillations with different spatial periods.

Dirac Spectrum

Let us further consider the case of Hamiltonian with Dirac spectrum:

$$H_k = -\boldsymbol{B}_k \cdot \hat{\boldsymbol{\sigma}}, \quad \varepsilon^\pm_k = \mp\sqrt{h^2 + (\lambda k)^2}. \tag{8}$$

This model describes, for example, chiral surface states of a 3D TI (the SOI parameters are $\chi = 1$, $\gamma = \pi$). Shown in Fig. 4a is the spectrum (8), which consists of two nearly linear bands separated by the gap $2h$. The fundamental difference from the previously considered parabolic-like spectrum is the additional electron-hole symmetry ($\mathcal{C}$-symmetry), which modifies the electron gas response to external perturbations[42–45].

Let us put the Fermi energy $\mu > 0$ above the charge neutrality point, so the lower (+) subband is completely filled while the upper (−) subband is filled partially. Our calculations show that the (+) subband does not

contribute to the response of z spin component ($\mathcal{F}_z^+ = 0$), while for the ($-$) subband the spin response function is the conventional 2D Lindhard function (the details of the calculations are given in the Supplementary Appendix B):

$$\mathcal{F}_z^-(q) = \frac{m_g}{4\pi}(1 - \Theta[q - 2k_-]\sqrt{1 - 4k_-^2/q^2}), \tag{9}$$

where $m_g = h/\lambda^2$ is an effective mass due to the spectrum gap, $k_- = \sqrt{\mu^2 - h^2}/\lambda$ is the Fermi wavevector. This result is rather interesting as the Lindhard function usually describes the susceptibility of a system with simple parabolic spectrum.

Another important feature of $\mathcal{F}_z^-$ given by (9) is that its magnitude does not depend on the Fermi energy μ. This is in contrast with the parabolic-like case, where the increase of μ leads to the suppression of spin response according to $\mathcal{F}_z^\pm \propto 1/\zeta_\pm$ at $\zeta_\pm \gg 1$. This effect is due to the density of states, which for the Dirac spectrum takes the form $\nu_-(\mu) = \mu/2\pi\lambda^2$. Upon the increase of the Fermi energy the suppression of spin z-projection (which is $h/2B_k \propto 1/\zeta_-$ at $\mu \gg h$) is exactly compensated by the increase of $\nu_-(\mu)$. For instance, considering the local coupling regime $\delta S_z = \varkappa_z V(\boldsymbol{r})$ the spin response is exactly determined by a product $\varkappa_z^- = \nu_-(\mu)h/2\mu = m_g/4\pi$ independent of μ.

The in-plane spin response also exhibits a number of peculiar features. For the functions $\mathcal{F}_\parallel^\pm(q)$ we obtained:

$$\mathcal{F}_\parallel^+(q) = \frac{m_g}{4\pi}\tan^{-1}(qa_0), \qquad \mathcal{F}_\parallel^-(q) = -\mathcal{F}_\parallel^+(q) + \frac{m_g}{4\pi}\Theta[q - 2k_-]\tan^{-1}\left(a_0\sqrt{\frac{q^2 - 4k_-^2}{1 + \zeta_-^2}}\right). \tag{10}$$

We note that there is a non-zero spin response from the completely filled ($+$) subband, and that $\mathcal{F}_\parallel^+/q$ remains finite even at $qa_0 \ll 1$. This is an unusual behavior, since no charge density response of the ($+$) subband can be induced in this case. Indeed, the interband transitions underlying the change of electron density are suppressed for a smooth potential $qa_0 \ll 1$ due to the finite band gap $2h$. On the contrary, the in-plane spin response originates from the spin precession driven by a drift electron flow, which remains finite in $\mathcal{C}$-symmetry systems even with gaped spectrum due to the Klein tunneling.

Considering the in-plane spin response from the upper ($-$) subband we note that the function $\mathcal{F}_\parallel^-(q)$ given by Eq. 10 contains both the μ-independent term opposite to that of ($+$) subband, and a μ-aware contribution responsible for the Friedel's oscillations with the spatial period $2k_-$. The in-plane spin response function $\mathcal{F}_\parallel = \mathcal{F}_\parallel^+ + \mathcal{F}_\parallel^-$ and its partial components $\mathcal{F}_\parallel^\pm$ are shown in Fig. 4b. The contributions of ($\pm$) subbands cancel each other at $q < 2k_-$ and $\mathcal{F}_\parallel$ turns to zero. Therefore, no in-plane spin response is induced by a long-range electrostatic perturbation when the Fermi level is in the upper subband.

The non-local spin response is also modified due to $\mathcal{C}$-symmetry. As can be seen in Fig. 4b the function $\mathcal{F}_\parallel(q) = \mathcal{F}_\parallel^+ + \mathcal{F}_\parallel^-$ saturates at $q \gg k_-$ instead of going to zero. However, as discussed above, the in-plane spin density responds to the potential gradient, so it is $\mathcal{F}_\parallel(q)/q$ which has the physical meaning and it indeed decays as $1/q$ at $q \to \infty$. In Fig. 4c we show the spatial spin pattern $\delta S_{z,\parallel}$ induced by a short-range potential $V(q) = \alpha_0 exp[-(qa/2)^2]$, a is the potential radius. It is worth mentioning that the magnitude of the in-plane spin response $\delta S_\parallel$ in the vicinity of a defect is far larger than in the parabolic spectra case due to the saturation of $\mathcal{F}_\parallel(q)$. This finding emphasizes a particularly high susceptibility of a chiral spin pattern in response to an electrostatic disorder in systems with Dirac spectrum.

Summary and Discussion

Our study suggests that the emergence of chiral spin textures in an electron gas driven by an electrostatic disorder is a universal phenomenon, which is expected in a variety of experimentally studied systems, such as DMS[40,46], thin films of ferromagnets[32,33], Bi_2Se_3 doped by magnetic impurities[30,31,47,48], or due to the proximity effect[49] with magnetic insulators[50], or ferromagnets[51,52]. The derived analytical expressions for the spin-density response functions can be used to qualitatively analyze the effect in these systems and to treat the interplay between the spin-orbit interaction and Zeeman spin splitting of carriers in particular. The latter is of special importance for the locality of spin response, as the theory reveals the existence of an additional universal scale $a_0 = \lambda/2h$, which triggers the spatial dispersion.

We believe, that there are diverse experimental approaches allowing to reveal the chiral perturbation of the 2DEG spin density. For instance, probing the chiral spin textures induced on a surface by means of spin-polarized scanning tunneling microscopy[53] would be a new tool to access the parameters of the electron gas. The chiral spin pattern in the 2DEG can also induce a chiral order of magnetic ions due to the exchange interaction between these subsystems. In particular, this effect can occur not only for the magnetic moments located in the same material, but also for those in a different layer of a heterostructure due to the proximity effect[49]. Thus a chiral ordering of the magnetization can be induced in various systems by electrical means via the modulation of 2DEG spin density, hence, being an alternative tool to create magnetic skyrmions and other chiral spin textures. Also, the considered mechanism is likely to be responsible for the recently observed topological Hall effect in TI and DMS[54–56]. Indeed, the topological Hall effect originates from the asymmetric scattering of electrons on chiral spin textures[16]. It has been shown that it is not limited to magnetic skyrmions possessing a topological charge but also expected for a broad range of chiral spin textures[16,57]. One possible scenario for the formation of such chiral spin textures in magnetic systems with spin-orbit interaction is suggested by the presented theory. As follows from our study, the chiral spin textures inevitably emerge nearby defects and other inhomogeneities of a real structure and eventually they can give rise to the topological Hall effect.

References

1. Wen, X. G., Wilczek, F. & Zee, A. Chiral spin states and superconductivity. *Phys. Rev. B* **39**, 11413, https://doi.org/10.1103/PhysRevB.39.11413 (1989).
2. Chen, X., Gu, Z.-C. & Wen, X.-G. Local unitary transformation, long-range quantum entanglement, wave function renormalization, and topological order. *Phys. Rev. B* **82**, 155138, https://doi.org/10.1103/PhysRevB.82.155138 (2010).
3. Batista, C. D., Lin, S.-Z., Hayami, S. & Kamiya, Y. Frustration and chiral orderings in correlated electron systems. *Reports on Prog. Phys.* **79**, 084504, https://doi.org/10.1088/0034-4885/79/8/084504 (2016).
4. Kallin, C. & Berlinsky, J. Chiral superconductors. *Reports on Prog. Phys.* **79**, 054502, https://doi.org/10.1088/0034-4885/79/5/054502 (2016).
5. Kalmeyer, V. & Laughlin, R. B. Equivalence of the resonating-valence-bond and fractional quantum Hall states. *Phys. Rev. Lett.* **59**, 2095–2098, https://doi.org/10.1103/PhysRevLett.59.2095 (1987).
6. Yang, K., Warman, L. & Girvin, S. Possible spin-liquid states on the triangular and Kagomé lattices. *Phys. Rev. Lett.* **70**, 2641, https://doi.org/10.1103/PhysRevLett.70.2641 (1993).
7. Kitaev, A. Anyons in an exactly solved model and beyond. *Annals Phys.* **321**, 2–111, https://doi.org/10.1016/j.aop.2005.10.005 (2006).
8. Volovik, G. E. Topology of chiral superfluid: Skyrmions, Weyl fermions, and chiral anomaly. *JETP Lett.* **103**, 140, https://doi.org/10.1134/S0021364016020144 (2016).
9. Lee, P. A. & Nagaosa, N. Gauge theory of the normal state of high-Tc superconductors. *Phys. Rev. B* **46**, 5621, https://doi.org/10.1103/PhysRevB.46.5621 (1992).
10. Bauer, B. *et al.* Chiral spin liquid and emergent anyons in a Kagome lattice Mott insulator. *Nat Commun* **5**, 5137, https://doi.org/10.1038/ncomms6137 (2014).
11. Messio, L., Bieri, S., Lhuillier, C. & Bernu, B. Chiral spin liquid on a Kagome antiferromagnet induced by the Dzyaloshinskii-Moriya interaction. *Phys. Rev. Lett.* **118**, 267201, https://doi.org/10.1103/PhysRevLett.118.267201 (2017).
12. Ye, J. *et al.* Berry phase theory of the anomalous Hall effect: Application to colossal magnetoresistance manganites. *Phys. Rev. Lett.* **83**, 3737, https://doi.org/10.1103/PhysRevLett.83.3737 (1999).
13. Chun, S. H., Salamon, M. B., Lyanda-Geller, Y., Goldbart, P. M. & Han, P. D. Magnetotransport in manganites and the role of quantal phases: theory and experiment. *Phys. Rev. Lett.* **84**, 757, https://doi.org/10.1103/PhysRevLett.84.757 (2000).
14. Bruno, P., Dugaev, V. K. & Taillefumier, M. Topological Hall effect and Berry phase in magnetic nanostructures. *Phys. Rev. Lett.* **93**, 096806, https://doi.org/10.1103/PhysRevLett.93.096806 (2004).
15. Neubauer, A. *et al.* Topological Hall effect in the A phase of MnSi. *Phys. Rev. Lett.* **102**, 186602, https://doi.org/10.1103/PhysRevLett.102.186602 (2009).
16. Denisov, K. S., Rozhansky, I. V., Averkiev, N. S. & Lähderanta, E. General theory of the topological Hall effect in systems with chiral spin textures. *Phys. Rev. B* **98**, 195439, https://doi.org/10.1103/PhysRevB.98.195439 (2018).
17. Hamamoto, K., Ezawa, M. & Nagaosa, N. Quantized topological Hall effect in skyrmion crystal. *Phys. Rev. B* **92**, 115417, https://doi.org/10.1103/PhysRevB.92.115417 (2015).
18. Fert, A., Reyren, N. & Cros, V. Magnetic skyrmions: advances in physics and potential applications. *Nat. Rev. Mater.* **2**, 17031, https://doi.org/10.1038/natrevmats.2017.31 (2017).
19. Wiesendanger, R. Nanoscale magnetic skyrmions in metallic films and multilayers: a new twist for spintronics. *Nat. Rev. Mater.* **1**, 16044, https://doi.org/10.1038/natrevmats.2016.44 (2016).
20. Soumyanarayanan, A. *et al.* Tunable room-temperature magnetic skyrmions in Ir/Fe/Co/Pt multilayers. *Nat. materials* **16**, 898, https://doi.org/10.1038/nmat4934 (2017).
21. Akosa, C. A., Tretiakov, O. A., Tatara, G. & Manchon, A. Theory of the Topological Spin Hall Effect in Antiferromagnetic Skyrmions: Impact on Current-Induced Motion. *Phys. Rev. Lett.* **121**, 097204, https://doi.org/10.1103/PhysRevLett.121.097204 (2018).
22. Yu, X. *et al.* Transformation between meron and skyrmion topological spin textures in a chiral magnet. *Nat.* **564**, 95, https://doi.org/10.1038/s41586-018-0745-3 (2018).
23. Bogdanov, A. N. & Yablonskii, D. Thermodynamically stable "vortices" in magnetically ordered crystals. *The mixed state of magnets. Zh. Eksp. Teor. Fiz* **95**, 178 (1989).
24. Bogdanov, A. & Hubert, A. Thermodynamically stable magnetic vortex states in magnetic crystals. *J. Magn. Magn. Mater.* **138**, 255–269, https://doi.org/10.1016/0304-8853(94)90046-9 (1994).
25. Jiang, W. *et al.* Direct observation of the skyrmion Hall effect. *Nat. Phys.* **13**, 162, https://doi.org/10.1038/nphys3883 (2017).
26. Tomasello, R. *et al.* A strategy for the design of skyrmion racetrack memories. *Sci. reports* **4**, 6784, https://doi.org/10.1038/srep06784 (2014).
27. Bessarab, P. F. *et al.* Lifetime of racetrack skyrmions. *Sci. Reports* **8**, 3433, https://doi.org/10.1038/s41598-018-21623-3 (2018).
28. Tokura, Y., Yasuda, K. & Tsukazaki, A. Magnetic topological insulators. *Nat. Rev. Phys.* **1**, 126, https://doi.org/10.1038/s42254-018-0011-5 (2019).
29. Okada, Y. *et al.* Direct observation of broken time-reversal symmetry on the surface of a magnetically doped topological insulator. *Phys. Rev. Lett.* **106**, 206805, https://doi.org/10.1103/PhysRevLett.106.206805 (2011).
30. Wei, P. *et al.* Exchange-coupling-induced symmetry breaking in topological insulators. *Phys. Rev. Lett.* **110**, 186807, https://doi.org/10.1103/PhysRevLett.110.186807 (2013).
31. Chen, Y. *et al.* Massive Dirac fermion on the surface of a magnetically doped topological insulator. *Sci.* **329**, 659–662, https://doi.org/10.1126/science.1189924 (2010).
32. Miron, I. M. *et al.* Current-driven spin torque induced by the Rashba effect in a ferromagnetic metal layer. *Nat. materials* **9**, 230, https://doi.org/10.1038/nmat2613 (2010).
33. Miron, I. M. *et al.* Perpendicular switching of a single ferromagnetic layer induced by in-plane current injection. *Nat.* **476**, 189, https://doi.org/10.1038/nature10309 (2011).
34. Manchon, A., Koo, H. C., Nitta, J., Frolov, S. & Duine, R. New perspectives for Rashba spin–orbit coupling. *Nat. materials* **14**, 871, https://doi.org/10.1038/nmat4360 (2015).
35. Zhou, L. *et al.* Observation of spin-orbit magnetoresistance in metallic thin films on magnetic insulators. *Sci. advances* **4**, eaao3318, https://doi.org/10.1126/sciadv.aao3318 (2018).
36. Liu, C.-X., Qi, X.-L., Dai, X., Fang, Z. & Zhang, S.-C. Quantum anomalous Hall effect in $Hg_{1-y}Mn_yTe$ quantum wells. *Phys. Rev. Lett.* **101**, 146802, https://doi.org/10.1103/PhysRevLett.101.146802 (2008).
37. Yu, R. *et al.* Quantized anomalous Hall effect in magnetic topological insulators. *Sci.* **329**, 61–64, https://doi.org/10.1126/science.1187485 (2010).
38. Chernyshov, A. *et al.* Evidence for reversible control of magnetization in a ferromagnetic material by means of spin-orbit magnetic field. *Nat. Phys.* **5**, 656, https://doi.org/10.1038/nphys1362 (2009).
39. Novik, E. G. *et al.* Band structure of semimagnetic $Hg_{1-y}Mn_yTe$ quantum wells. *Phys. Rev. B* **72**, 035321, https://doi.org/10.1103/PhysRevB.72.035321 (2005).
40. Jungwirth, T. *et al.* Spin-dependent phenomena and device concepts explored in (Ga;Mn)As. *Rev. Mod. Phys.* **86**, 855, https://doi.org/10.1103/RevModPhys.86.855 (2014).
41. Li, H., Wang, X., Dogan, F. & Manchon, A. Tailoring spin-orbit torque in diluted magnetic semiconductors. *Appl. Phys. Lett.* **102**, 192411, https://doi.org/10.1063/1.4806981 (2013).

42. Hwang, E. H. & Das Sarma, S. Dielectric function, screening, and plasmons in two-dimensional graphene. *Phys. Rev. B* **75**, 205418, https://doi.org/10.1103/PhysRevB.75.205418 (2007).
43. Wunsch, B., Stauber, T., Sols, F. & Guinea, F. Dynamical polarization of graphene at finite doping. *New J. Phys.* **8**, 318, https://doi.org/10.1088/1367-2630/8/12/318 (2006).
44. Zhu, J.-J., Yao, D.-X., Zhang, S.-C. & Chang, K. Electrically controllable surface magnetism on the surface of topological insulators. *Phys. Rev. Lett.* **106**, 097201, https://doi.org/10.1103/PhysRevLett.106.097201 (2011).
45. Checkelsky, J. G., Ye, J., Onose, Y., Iwasa, Y. & Tokura, Y. Dirac-fermion-mediated ferromagnetism in a topological insulator. *Nat. Phys.* **8**, 729, https://doi.org/10.1038/nphys2388 (2012).
46. Gaj, J. A. & Kossut, J. *Introduction to the Physics of Diluted Magnetic Semiconductors* (Springer, 2010).
47. Kou, X. *et al.* Magnetically doped semiconducting topological insulators. *J. Appl. Phys.* **112**, 063912, https://doi.org/10.1063/1.4754452 (2012).
48. Watson, M. D. *et al.* Study of the structural, electric and magnetic properties of Mn-doped Bi2Te3 single crystals. *New J. Phys.* **15**, 103016, https://doi.org/10.1088/1367-2630/15/10/103016 (2013).
49. Žutić, I., Matos-Abiague, A., Scharf, B., Dery, H. & Belashchenko, K. Proximitized materials. *Mater. Today* **22**, 85, https://doi.org/10.1016/j.mattod.2018.05.003 (2018).
50. Vobornik, I. *et al.* Magnetic proximity effect as a pathway to spintronic applications of topological insulators. *Nano Lett.* **11**, 4079, https://doi.org/10.1021/nl201275q (2011).
51. Lv, Y. *et al.* Unidirectional spin-Hall and Rashba- Edelstein magnetoresistance in topological insulator-ferromagnet layer heterostructures. *Nat. communications* **9**, 111, https://doi.org/10.1038/s41467-017-02491-3 (2018).
52. Lee, J. S. *et al.* Engineering the breaking of time-reversal symmetry in gate-tunable hybrid ferromagnet/topological insulator heterostructures. *npj Quantum Mater.* **3**, 51, https://doi.org/10.1038/s41535-018-0123-2 (2018).
53. Wiesendanger, R. Spin mapping at the nanoscale and atomic scale. *Rev. Mod. Phys.* **81**, 1495, https://doi.org/10.1103/RevModPhys.81.1495 (2009).
54. Jiang, J. *et al.* Crossover of quantum anomalous Hall to topological Hall effect in magnetic topological insulator sandwich heterostructures. *Prepr.* at https://arxiv.org/abs/1901.07611 (2019).
55. Liu, C. *et al.* Dimensional crossover-induced topological Hall effect in a magnetic topological insulator. *Phys. Rev. Lett.* **119**, 176809, https://doi.org/10.1103/PhysRevLett.119.176809 (2017).
56. Oveshnikov, L. N. *et al.* Berry phase mechanism of the anomalous Hall effect in a disordered two-dimensional magnetic semiconductor structure. *Sci. Reports* **5**, 17158, https://doi.org/10.1038/srep17158 (2015).
57. Rozhansky, I. V., Denisov, K. S., Lifshits, M. B., Averkiev, N. S. & Lähderanta, E. Topological and chiral spin Hall effects. *Phys. Status Solidi (b)* 1900033, https://doi.org/10.1002/pssb.201900033 (2019).

Acknowledgements

Author Contributions

K.S.D., I.V.R. and N.S.A. formulated the physical problem, carried out the analytical calculations of spin-density correlation functions and wrote the paper. K.S.D., I.V.R. and E.L. carried out the analysis of the real space spin density response.

Additional Information

Supplementary information accompanies this paper at https://doi.org/10.1038/s41598-019-47274-6.

Competing Interests: The authors declare no competing interests.

Publisher's note: Springer Nature remains neutral with regard to jurisdictional claims in published maps and institutional affiliations.